Structure and properties of fiber-reinforced polypropylene prepared by direct incorporation of aqueous solution of poly(vinyl alcohol)

Riho Nishikawa,*,† Norifumi Aridome,‡ Naoki Ojima,‡ Masayuki Yamaguchi*,†

†School of Materials Science, Japan Advanced Institute of Science and Technology, 1-1 Asahidai, Nomi, Ishikawa 923-1292, Japan

‡Setsunan Kasei Co., Ltd. 2-2-1 Techno Stage, Izumi, Osaka 594-1144, Japan

*Corresponding author
E-mail address: s1820025@jaist.ac.jp (Riho Nishikawa),
m_yama@jaist.ac.jp (Masayuki Yamaguchi)
Address: 1-1 Asahidai, Nomi, Ishikawa 923-1292 JAPAN
Phone: +81-761-51-1621
Fax: +81-761-51-1149

ABSTRACT

Poly(vinyl alcohol) (PVA) is immiscible with most conventional plastics and also unsuitable for melt processing owing to its extensive hydrogen bonding. Therefore, there have been few studies concerning the melt-mixing of PVA with standard plastics. The present paper describes a novel technique for producing isotactic polypropylene (PP) composites containing PVA fibers by directly introducing an aqueous solution of PVA into molten PP from an injection nozzle in a twin-screw extruder having a wide venting port. The PVA fibers were found to be dispersed homogeneously in the composites obtained by this method. Furthermore, an injection-molded product made from this composite exhibited an increased modulus, high yield strength, and high heat distortion temperature. These properties are attributed to the significant degree of orientation of both the PP chains and the PVA fibers. The nucleating action of the PVA fibers oriented in the flow direction is responsible for the structure of the composite, which in turn results in attractive properties.

Keywords: Poly(vinyl alcohol); Fiber-reinforced polymer; Mechanical property

1. INTRODUCTION

Fiber-reinforced plastics have been developed since the early stages of the plastics industry. One of the main aims was, of course, the replacement of ceramics and metals. Such efforts were particularly successful in the field of engineering plastics containing glass fibers, owing to their excellent specific modulus and strength values. Recently, there has been another wave of polymer composites containing fibrous materials because of the development of advanced fibers such as aramid fibers [1,2], carbon fibers [3–6], carbon nanotubes [7–12], and cellulose nanofibers [13–15]. These fibrous materials have great potential to provide the rigidity and toughness required for various plastics. Of particular note is the impact of small-diameter fibers—which act as nucleating agents for the matrix polymer—on the structure and properties of crystalline polymers. In such cases, a shish kebab-like structure—in which the fibrous materials behave as the skewer—is easily developed, resulting in a high modulus in the flow direction [12,16–18].

The present study focused on poly(vinyl alcohol) (PVA) fibers because these have an extremely high modulus and are very strong [19]. These properties may be attributed to the small diameter of the polymer chains, resulting in a large number of chains per unit area of fiber, and the strong intermolecular interactions that result from hydrogen bonding. In fact, one of the main applications of PVA fibers is as toughness modifiers for cementitious composites [20,21]. Recently, the properties of PVA fiber-reinforced rubberized concrete were examined by Wang et al. [22], who reported that the specific strength of the composite was greatly improved owing to the light weight of the PVA fibers. Of course, such performance enhancement is also expected for plastics although, to the best of our knowledge, only a few studies have been carried out on polymer composites with PVA fibers [23–26]. Recently, Sobczak et al. reported the mechanical properties of polypropylene (PP) composites with PVA fibers and found that these composites had high mechanical toughness [26]. A similar study

was reported using epoxy resin by Phong et al. [24]. In these studies, PVA fibers were directly mixed with the plastic. In general, however, the homogeneous dispersion of long hydrophilic fibers in a hydrophobic polymer melt is problematic on an industrial scale.

Fiber-dispersed polymer composites can be prepared by melt-mixing two immiscible polymers in a rapid solidification process [27]. Typically, the shape of a dispersed polymer in another polymer matrix is determined by the viscosity ratio, interfacial tension, and processing conditions such as the flow field and the solidification process. When the dispersed polymer has a much lower viscosity than the matrix, it adopts a fibrous shape under flow in an extruder. If the blend is solidified before Rayleigh disturbance takes effect, a fiber-dispersed polymer is obtained [18,28–31].

PVA is immiscible with most plastics because it is hydrophilic [32,33]. Moreover, this polymer undergoes strong internal hydrogen bonding, which prohibits melt processing. Therefore, it is almost impossible to mix PVA with a conventional plastic in the molten state, although a great improvement in rigidity would be expected owing to the high modulus of the resulting composite [19]. On this basis, the present paper proposes a novel technique for the production of polymer composites containing PVA fibers, in which an aqueous solution of PVA is directly inserted into a molten polymer using a twin-screw extruder equipped with a liquid-injection nozzle to feed the solution. Importantly, the venting port of the extruder used in this work is wide enough to completely remove the moisture in the original solution.

2. EXPERIMENTAL SECTION

2.1 Materials

The polymers used in the present research were PP with a melt mass flow rate (MFR) of 21 g/10 min at 230 °C (Novatec-PP MA1B; Japan Polypropylene Corp., Tokyo, Japan) and PVA, which contained a small amount of 1-butene-3,4-diol as a comonomer (Nichigo G-

Polymer OKS-1011; Mitsubishi Chemical Corp., Tokyo, Japan). The PVA had a degree of saponification of more than 98% and a degree of polymerization of 300. The melting points of the PP and PVA were 165 °C and 206 °C, respectively.

2.2 Sample preparation

A co-rotating twin-screw extruder (TEM37SS; Toshiba Machine Co., Ltd., Numazu, Japan) was used in the present study, as illustrated in Fig. 1. The screw rotation speed was 150 rpm. The PP pellets were fed into the hopper using a loss-in-weight feeder and melted prior to entering the area near the liquid-injection nozzle. An aqueous solution of PVA (20 wt.% PVA) was then injected directly from the nozzle into the molten PP by a metering pump. The ratio of PP and the aqueous solution of PVA (20 wt.% PVA) was 90/50 (w/w). The barrel temperature was maintained at 200 °C, except for the areas near the hopper and injection nozzle, the latter of which was maintained at 150 °C. Water was allowed to evaporate from the vacuum venting ports, which were wider than that of a conventional extruder. After mixing sufficiently, the PP/PVA (90/10, w/w) strands extruded from the circular die were cooled in a water bath, then pelletized using a strand cutter. The majority of the water originally in the material evidently evaporated because the extruded strands had no bubbles. The same procedure was also performed using PP together with pure water instead of the PVA solution.

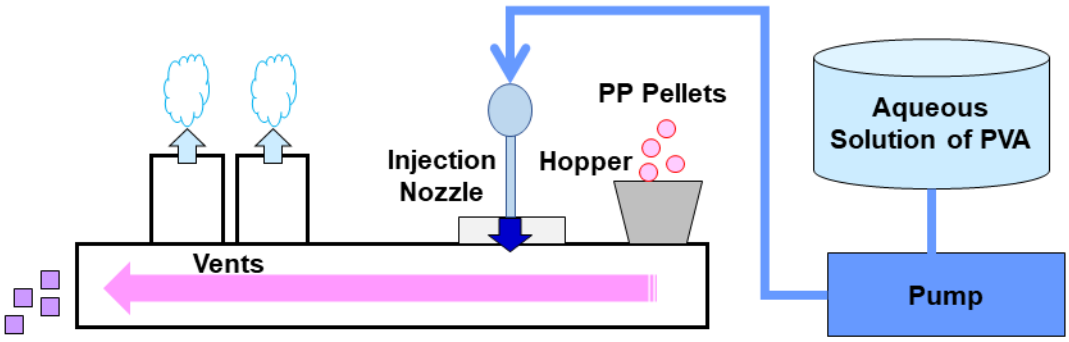

Fig. 1. A schematic illustration of the co-rotating twin-screw extruder used in the present study.

After the obtained pellets were dried, 4-mm-thick dumbbell-shaped specimens (10 mm in width and 150 mm in length) were prepared using an injection-molding machine (SI-80IV-D150B 200 t; Toyo Machinery & Metal Co., Ltd., Akashi, Japan). The barrel and nozzle were maintained at 175 °C during the molding process. A PVA film was also prepared using a solution casting method in which PVA powder was dissolved in hot water at 80 °C with stirring. After 4 h, the solution was transferred to a Petri dish and the water evaporated at 80 °C to form a thin film for a night. Then it was vacuum dried at 23 °C for a night.

2.3 Measurements

The dispersion of PVA in each composite was examined using polarizing optical microscopy (POM) (crossed polars configuration) (Leica DMLP; Leica Microsystems, Ltd., Wetzlar, Germany) in conjunction with a hot stage (Mettler FP90; Mettler Toledo, Inc., Columbus, OH) at 180, 200, and 230 °C. In addition, the PP/PVA composites were immersed

in hot xylene for 4 h at 140 °C to remove the PP fraction, after which the insoluble portions were dried and examined by POM without the crossed polars configuration at 23 °C.

The angular frequency dependence of the oscillatory shear modulus of each specimen was determined using a cone-and-plate rheometer (AR2000ex; TA Instruments, Inc., New Castle, DE) at 180 °C under a nitrogen atmosphere. The diameter of the cone was 25 mm, the cone angle was 4°, and the angular frequency ranged from 0.01 to 628.3 rad/s. The shear stress and the primary normal stress difference under steady-state shear flow were also evaluated as functions of the shear rate using the same rheometer at 180 °C.

The steady-state shear viscosity of each sample was measured at 180 °C using a capillary rheometer (140 SAS-2002; Yasuda Seiki Seisakusho, Ltd., Nishinomiya, Japan), employing a circular die with a length (L)-to-diameter (D) ratio of 10/1 (mm) and an entrance angle of 2π. The Bagley correction was not applied because the end pressure drop was low owing to the low viscosity of the specimens, although the Rabinowitsch correction was used to account for non-Newtonian behavior.

The thermal properties were evaluated using differential scanning calorimetry (DSC) (DSC8500; PerkinElmer, Inc., Waltham, MA) under a nitrogen atmosphere. In each trial, an approximately 10 mg portion of a pellet was encapsulated in an aluminum pan and heated to 190 °C. After holding the sample at that temperature for 10 min to melt the PP completely, the sample was cooled to 50 °C at 10 °C/min to assess the crystallization temperature. Isothermal crystallization was also evaluated. In these experiments, after melting the PP as described above, the sample was cooled to a specific crystallization temperature (128, 130, or 132 °C) at 60 °C/min and kept at that temperature. The heat of fusion obtained during the first heating of each injection-molded specimen at 10 °C/min was used to evaluate the degree of PP crystallinity.

Scanning electron microscopy (SEM) (TM3030Plus; Hitachi, Ltd., Tokyo, Japan) was used to examine the morphologies of the injection-molded specimens. Prior to observations, the cryogenically fractured surfaces were sputter-coated with Pt–Pd.

Two-dimensional wide-angle X-ray diffraction (2D-WAXD) patterns of the injection-molded specimens were collected using an X-ray diffraction (XRD) instrument (SmartLab; Rigaku Corp., Akishima, Japan) with an imaging plate. During these trials, specimens were exposed to a graphite-monochromatized Cu Kα radiation beam, generated at 45 kV and 200 mA, for 30 s. Conventional one-dimensional WAXD (1D-WAXD) analyses were also performed in the reflection mode at a scanning speed of 10°/min by reflecting a graphite-monochromatized Cu Kα beam generated at 40 kV and 30 mA from the injection-molded specimens.

Orientation birefringence was measured using POM (crossed polars configuration) together with a tilting compensator. Prior to each analysis, a film specimen with a 40 μm thickness was cut from the injection-molded specimen with a microtome (RX-860; Yamato Kohki Industrial Co., Ltd., Asaka, Japan) at approximately -80 °C.

The crystallization behavior of the PP was evaluated using POM (crossed polars configuration and inserting a full-wave plate) in conjunction with the hot stage. After holding the sample at 180 °C for 10 min to melt the PP completely, the material was cooled to the crystallization temperature at 30 °C/min and the resulting isothermal crystallization was monitored.

The effect of temperature on the dynamic tensile moduli of the samples was evaluated using dynamic mechanical analysis (DMA) (Rheogel-E4000; UBM Co., Ltd., Muko, Japan) in the tensile test mode. The temperature range was from -50 to 180 °C, the frequency was 10 Hz, and the heating rate was 2 °C/min. A rectangular sample was cut from each injection-molded

specimen and from the PVA film and an oscillatory strain was applied parallel to the flow direction.

Each injection-molded specimen was also subjected to tensile and three-point bending testing using a universal testing machine (Autograph AG-X; Shimadzu Corp., Kyoto, Japan). The tensile testing was performed according to Japanese Industrial Standard (JIS) K7162 (which in turn is based on ISO 527-2) at 23 °C, while the three-point bending testing was performed according to JIS K7171 (which is based on ISO 178), also at 23 °C. Each measurement was performed three times and the average values are reported.

The heat distortion temperature (HDT) of each injection-molded specimen was determined under a pressure of 1.8 MPa using a specialized apparatus (HDT Tester 3M-2; Toyo Seiki Seisaku-sho, Ltd., Tokyo, Japan) according to JIS K7191-1 and JIS K7191-2 (which are based on ISO 75-1 and ISO 75-2, respectively).

3. RESULTS AND DISCUSSION

3.1 Characterization of the composite

A small amount of the PP/PVA (90/10) composite was used to evaluate the dispersion state and the shape of the PVA in the molten PP, based on observations via POM with a crossed polars configuration at 180 °C. After melting the PP, the sample was slightly compressed between a glass slide and cover to produce a thin film. As shown in Fig. 2, the PVA had been formed into fiber-like shapes, each with an approximate diameter of 5 μm. The PVA fibers were dispersed randomly as a result of the sample preparation method before the observation. It should be noted that they have no agglomeration even before the injection-molding, which will be discussed later. Moreover, no large particles were detected, suggesting that the mixing in the extruder was effective. The fibers continued to be evident even at 200 °C but became spherical at 230 °C (i.e., above the melting point, T_m, of PVA). Immersion experiments were

also performed to obtain PVA fibers for examination. In these trials, hot xylene was used to dissolve the PP while leaving the PVA unaffected. The majority of the insoluble portion of each specimen was found to comprise fibrous shapes and Fig. 3 presents an optical microscopy image (without crossed polars) of one such sample.

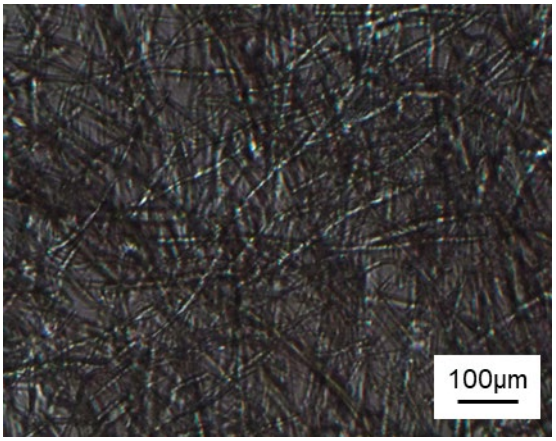

Fig. 2. A POM image (acquired using a crossed polars configuration) of a PP/PVA (90/10) sample at 180 ℃.

Fig. 3. An optical microscopy image of a PVA fiber.

The rheological properties of the specimens in the molten state were evaluated using a cone-and-plate rheometer. Fig. 4 shows the angular frequency ω dependence of the oscillatory shear moduli (the storage modulus, G', and loss modulus, G'') of pure PP and of a PP/PVA specimen at 180 °C. As the figure illustrates, both moduli of the pure PP decreased with decreasing frequency, which is a typical behavior in the rheological terminal region of a simple polymer melt (i.e., $G' \propto \omega^2$ and $G'' \propto \omega$). In contrast, the slope of the G' data acquired from the PP/PVA was less than that of the pure PP data, especially in the low frequency region. This

difference is attributed to the network structure of the PVA fibers, which is known to occur in fiber dispersion systems [12,16,30,34]. Specifically, the interdigitated structure of the fibers was responsible for the evident plateau in the modulus plot.

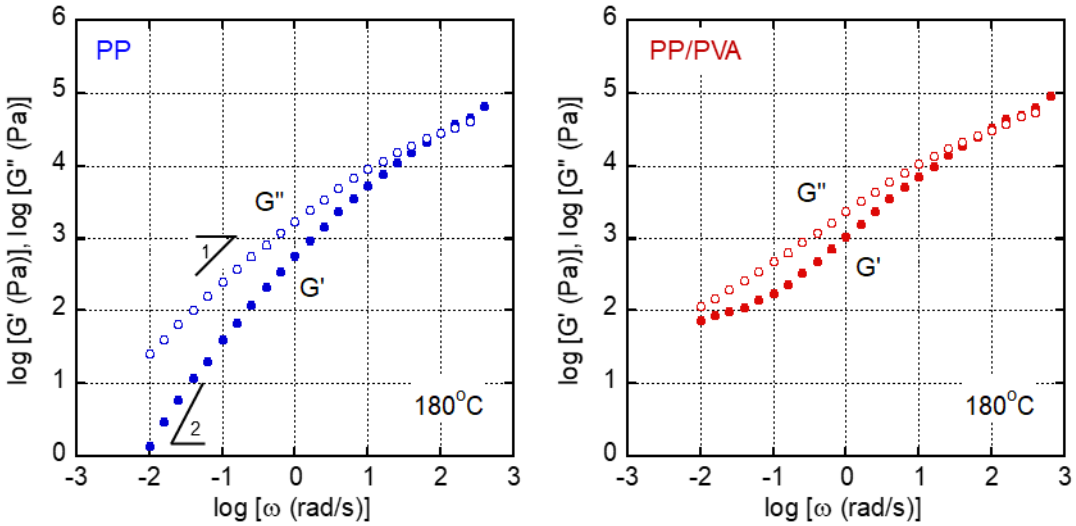

Fig. 4. The shear storage moduli G' (closed circles) and loss moduli G'' (open circles) of various specimens as functions of angular frequency ω at 180 °C.

The steady-state shear properties of the materials, including the primary normal stress difference, N, and shear stress, σ, were evaluated using the cone-and-plate rheometer, and Fig. 5 plots the resulting data against the shear rate, $\dot{\gamma}$, for both pure PP and PP/PVA at 180 °C. It is apparent that both N and σ increased with increases in $\dot{\gamma}$ and that the PP/PVA showed particularly high N values whereas the σ values obtained for the PP/PVA were similar to those for the pure PP. These results are in agreement with the linear viscoelastic properties shown in Fig. 4. To clarify the viscoelastic balance of the PP/PVA, N was plotted against σ for both the PP/PVA and pure PP, as shown in Fig. 6. The values obtained from the PP/PVA appeared above those for the pure PP, demonstrating that the addition of the PVA fibers provided increased elasticity to the molten PP [35].

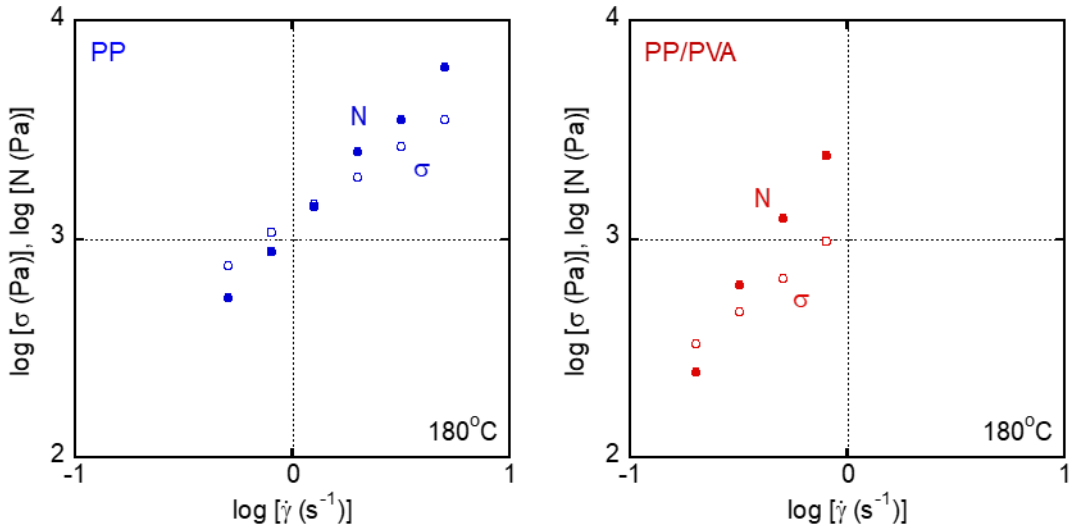

Fig. 5. The steady-state shear properties primary normal stress difference, N (closed circles), and shear stress, σ (open circles), of various samples as functions of the shear rate, $\dot{\gamma}$, at 180 °C.

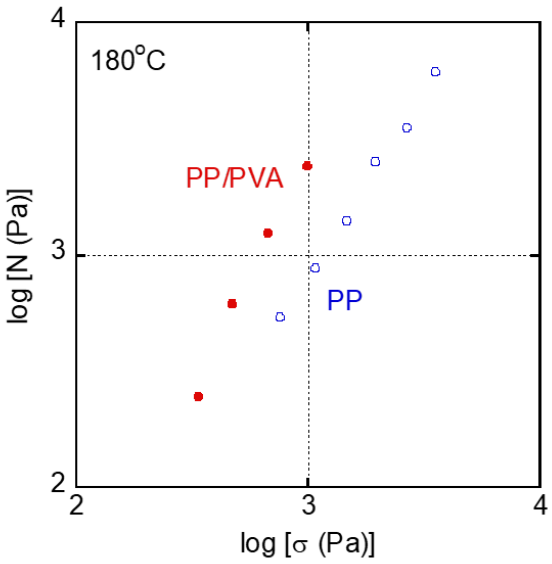

Fig. 6. The primary normal stress difference, N, plotted against the shear stress, σ, for PP (open circles) and PP/PVA (90/10) (closed circles).

Fig. 7 presents the flow curves acquired for these materials using a capillary rheometer. Specifically, the apparent shear stress values at the wall, σ_w, are plotted against the shear rate, $\dot{\gamma}$. It is important to note that these data indicate that the steady-state shear stress was barely affected by the addition of the PVA, presumably because of the orientation of the PVA fibers in the flow direction. It has been reported that viscosity increases during shear flow are reduced once such fibers are oriented in the flow direction [12,30,36].

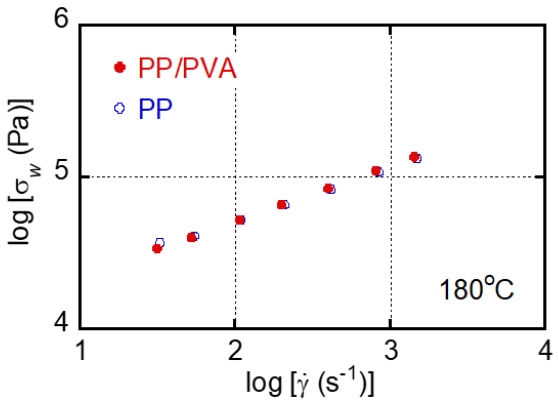

Fig. 7. Steady-state shear stress values at the wall, σ_w, plotted against the shear rate, $\dot{\gamma}$, during capillary extrusion at 180 °C for PP (open circles) and PP/PVA (90/10) (closed circles).

Fig. 8 provides the cooling curves acquired from DSC analyses of the samples at a cooling rate of 10 °C/min. The peak temperatures within these heat flow plots (corresponding to the crystallization temperatures) were 115.1 °C for the PP and 124.6 °C for the PP/PVA. Prior to the measurements, the thermal history of the PP was erased by heating at 190 °C for 10 min. At this temperature, which is lower than the T_m of PVA, the PVA remained in a fibrous morphology, as confirmed by POM observations. Considering that the pure PP had the same processing history, these results indicate that the PVA fibers acted as nucleating agents for the PP.

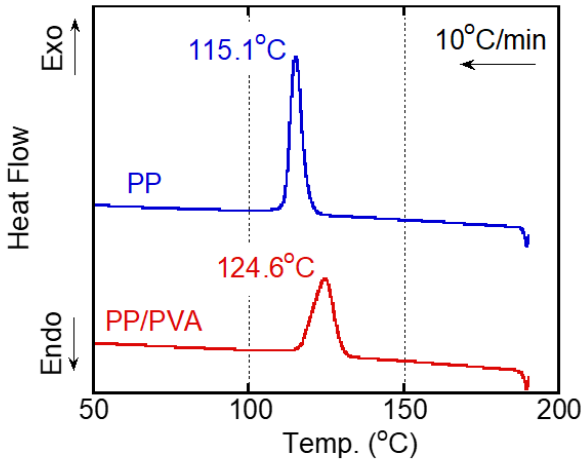

Fig. 8. DSC cooling curves obtained at 10 °C/min.

Fig. 9 shows the DSC curves acquired during the isothermal crystallization of samples at various crystallization temperatures, T_c. Note that the time at which the sample reaches T_c is set to 0 min in the figure. As shown in the figure, the PP/PVA exhibits a shorter induction period. Together with the non-isothermal data in Fig. 8, these results provide evidence that the PVA fibers act as nucleating agents for the PP. At the isothermal crystallization at 130 °C, the heat for crystallization of the PP was 102 J/g, while that of the PP/PVA was 91 J/g. This is reasonable because the weight fraction of PP in the blend was 90%.

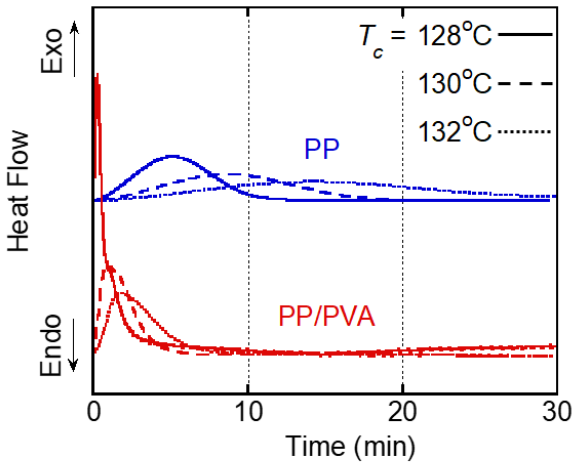

Fig. 9. DSC curves acquired during isothermal crystallization at 128, 130, and 132 °C.

The Avrami parameter, K, and Avrami exponent, n, were calculated based on the Avrami equation (1) [37–40]:

$$1 - V_c(t) = \exp(-Kt^n), \qquad (1)$$

where $V_c(t)$ is the relative volume fraction of crystallized material normalized by the maximum crystallization volume and n is the Avrami exponent. Fig. 10 shows the Avrami plots obtained from the double logarithmic equation (2):

$$\log\left[-\ln\left(1 - V_c(t)\right)\right] = \log K + n \log t. \qquad (2)$$

The results are summarized in Table 1 and the $\log K$ values are plotted against T_c in Fig. 11. These data demonstrate that K was increased by lowering T_c and by the addition of the PVA fibers. Furthermore, the values of n for the pure PP were barely affected by variations in T_c, whereas those for the PP/PVA were decreased with decreases in T_c. As a result, the smallest n value was obtained in the case of the PP/PVA specimen crystallized at 128 °C. Based on the classical Avrami theory [38], a smaller n value demonstrates that the PP chains crystallized along the PVA fibers.

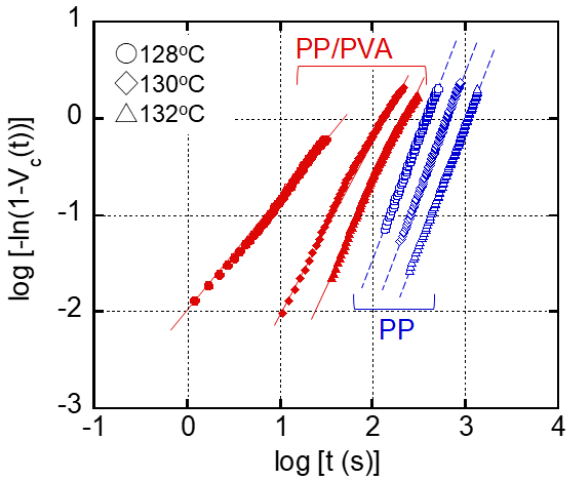

Fig. 10. Avrami plots at various crystallization temperatures for PP (open symbols) and PP/PVA (90/10) (closed symbols).

Table 1. Avrami parameter *K* and Avrami exponent *n*.

Temperature (°C)	Parameters	PP	PP/PVA (90/10)
128	*K*	2.8×10^{-7}	8.5×10^{-3}
	n	2.5	1.3
130	*K*	6.5×10^{-8}	1.9×10^{-4}
	n	2.6	1.8
132	*K*	2.3×10^{-8}	2.4×10^{-5}
	n	2.5	2.0

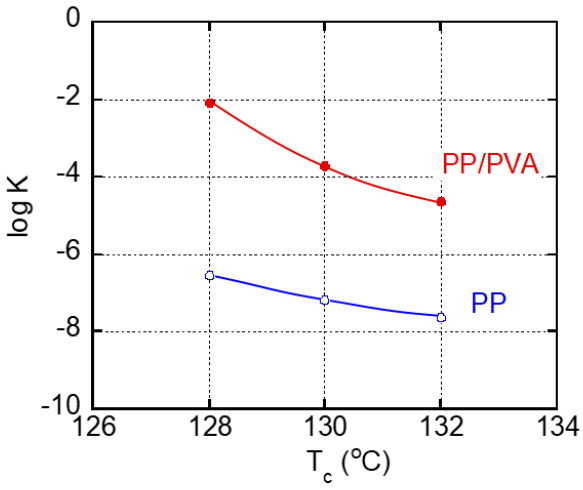

Fig. 11. The Avrami parameter, K, as a function of the crystallization temperature, T_c, for PP (open circles) and PP/PVA (90/10) (closed circles).

3.2 Characterization of the injection-molded specimens

The cryofractured surfaces of the skin layer of an injection-molded PP/PVA specimen were observed by scanning electron microscopy (SEM). The samples were found to be fractured along various planes (i.e., the machine direction (MD), transverse direction (TD), and normal/neutral direction (ND)), as indicated in Fig. 12. The average diameter of the fibers is estimated to be approximately 5 μm based on the SEM image of the TD–ND plane, which corresponds to the value obtained from the POM images (Figs. 2 and 3). This was as expected because the shape of the PVA fibers was determined by the extruder. Moreover, these images confirm that fibrous dispersions without interdigitated structure were present in the MD–TD and MD–ND planes, whereas circular dispersions were observed in the TD–ND plane. That is, the majority of the fibers were oriented along the MD. These results demonstrate that the PVA fibers were primarily oriented along the flow direction, suggesting that there was no agglomeration in both the extruded pellets and injection-molded specimens.

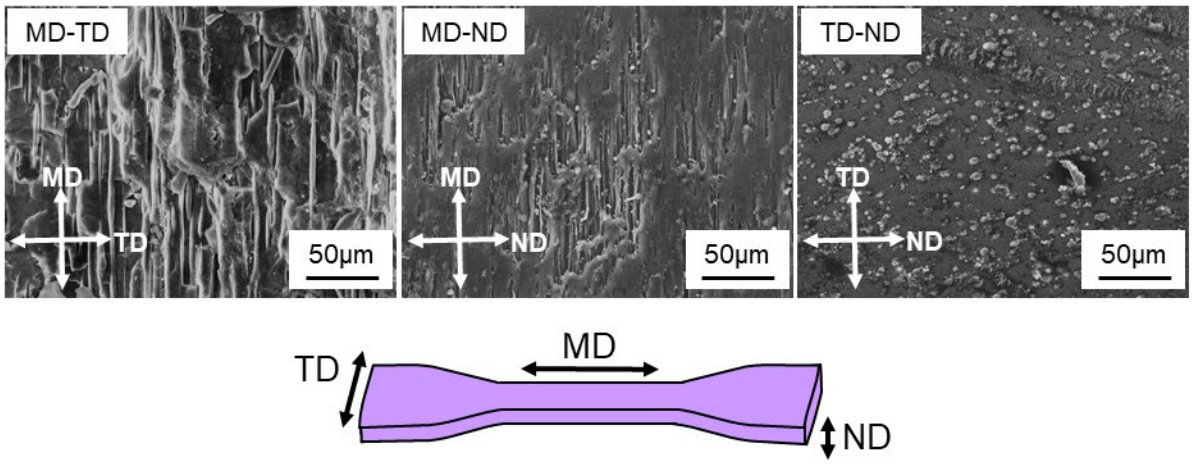

Fig. 12. SEM images of the cryofractured surfaces of an injection-molded PP/PVA (90/10) specimen. The schematic below the images indicates the directions associated with the notations MD, TD, and ND.

Fig. 13 shows the initial DSC heating curves acquired from the injection-molded specimens between 25 and 250 °C at a heating rate of 10 °C/min. Each sample was prepared by cutting the injection-molded specimen perpendicular to its wide surface (i.e., the TD-ND plane) so as to include both skin and core layers. The T_m values for the pure PP and PP/PVA samples were determined to be in the vicinity of 166 °C, and so were typical for PP. However, in the case of the PP/PVA specimen, a small peak was also detected close to 206 °C, which is the T_m of PVA. Heat of fusion, $\Delta H_{f\text{-}s}$, values were determined from these data and are provided in the figure. The degree of crystallization, χ, per unit mass of PP was calculated using the equation:

$$\chi = \frac{\Delta H_{f-s}}{\Delta H_{f-p}} \times \frac{1}{W} \times 100\ (\%), \qquad (3)$$

where $\Delta H_{f\text{-}p}$ is the heat of fusion for a perfect crystal, with a value of 209 J/g for PP [41], and W is the mass fraction of PP (i.e., 1.0 for the pure PP and 0.9 for the PP/PVA). The degree of crystallization was determined to be 43% for both the pure PP and PP/PVA, suggesting that the addition of the PVA fibers did not affect the crystallinity of the PP.

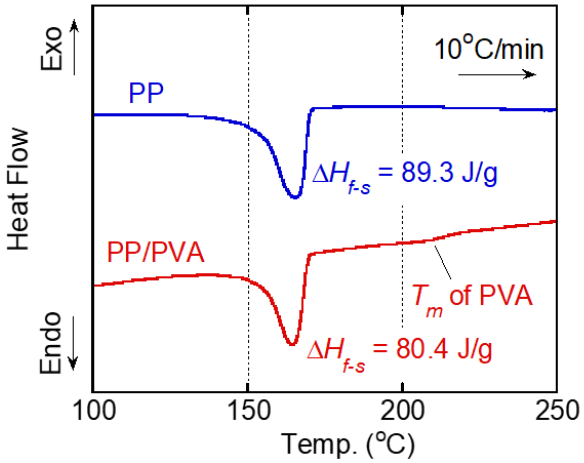

Fig. 13. DSC heating curves acquired at 10 °C/min for the injection-molded specimens.

Fig. 14 shows the through view 2D-WAXD images acquired with the X-ray beam passing through the MD–TD plane of each injection-molded specimen. It should be noted that, because the beam passed through the entire 4 mm-thick specimen, each diffraction peak was broadened. However, as indicated by the strong peaks on the equator that are denoted by the arrows and attributable to the (110), (040), and (130) planes of α-form crystals (the numerals in brackets are the Miller indices), the PP chains were predominantly oriented in the flow direction. Furthermore, the peaks generated by the PP/PVA were narrower than those produced by the pure PP. This phenomenon is discussed in detail further on.

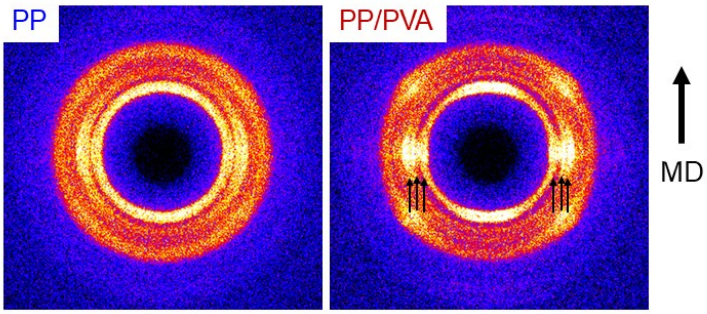

Fig. 14. 2D-WAXD images of the injection-molded specimens.

Fig. 15 presents the 1D-WAXD 2θ profiles obtained in the reflection mode for the injection-molded specimens. The three distinct peaks evident in the figure are attributable to the (110), (040), and (130) planes of the α monoclinic crystalline form of PP, and are easily discernable from the broad amorphous background. A strong diffraction peak is also present at 16.1° for both specimens, attributable to the β trigonal crystalline form of PP. This morphology can result from shear-induced directional crystallization in a temperature gradient field or from the addition of specific nucleating agents [42–46]. The relative proportion of β-form crystals has typically been determined using the parameter K_β, which was defined by Turner-Jones et al. [47] as:

$$K_\beta = \frac{I_{(110)\beta}}{I_{(110)\alpha} + I_{(040)\alpha} + I_{(130)\alpha} + I_{(110)\beta}}, \qquad (4)$$

where $I_{(110)\beta}$ is the integral intensity of the peak due to the (110) plane of the β-form crystals and $I_{(110)\alpha}$, $I_{(040)\alpha}$, and $I_{(130)\alpha}$ are the integral intensities of the peaks due to the (110), (040), and (130) planes of the α-form crystals, respectively. The K_β value for the pure PP was determined to be 0.17, whereas that for the PP/PVA was 0.10. Therefore, the PVA fibers have no capacity to promote the generation of β-form crystals.

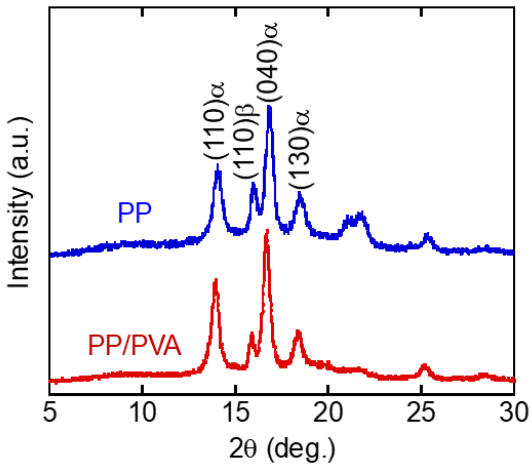

Fig. 15. The 1D-WAXD 2θ profiles for the injection-molded specimens.

Fig. 16 shows the azimuthal distributions of the (040) α plane as obtained from the 2D-WAXD images in Fig. 14, which are preferentially used to characterize the chain orientation of PP [48]. Both the PP and PP/PVA specimens produced strong peak intensities at 90° and 270° (i.e., on the equator), suggesting that the PP chains were predominantly oriented in the flow direction of the PP/PVA. The degree of orientation, A, was estimated from the azimuthal distribution using the equation:

$$A = \frac{360 - \sum w_i}{360} \times 100, \quad (5)$$

where w_i is the full width at half maximum.

The Hermans' orientation function, f, defined as

$$f = \frac{3\langle \cos^2 \phi \rangle - 1}{2}, \quad (6)$$

was calculated using the Wilchinsky method via the equation [48–51]:

$$\langle \cos^2 \phi \rangle = 1 - 1.090\langle \cos^2 \varphi_{110} \rangle - 0.901\langle \cos^2 \varphi_{040} \rangle. \quad (7)$$

Here, ϕ is the average angle that a segment makes with the MD and $<\cos^2\varphi_{110}>$ and $<\cos^2\varphi_{040}>$ are calculated using the equation [50,51]:

$$\langle \cos^2 \varphi_{hkl} \rangle = \frac{\int_0^{\pi} I(\varphi_{hkl}) \cos^2 \varphi_{hkl} \sin \varphi_{hkl} \, d\varphi_{hkl}}{\int_0^{\pi} I(\varphi_{hkl}) \sin \varphi_{hkl} \, d\varphi_{hkl}}, \qquad (8)$$

where $I(\varphi_{hkl})$ is the intensity of the (hkl) plane at the azimuthal angle φ. It is apparent from the A and f values, which are provided in the figure, that the orientation of the PP chains was greatly enhanced by the addition of the PVA fibers.

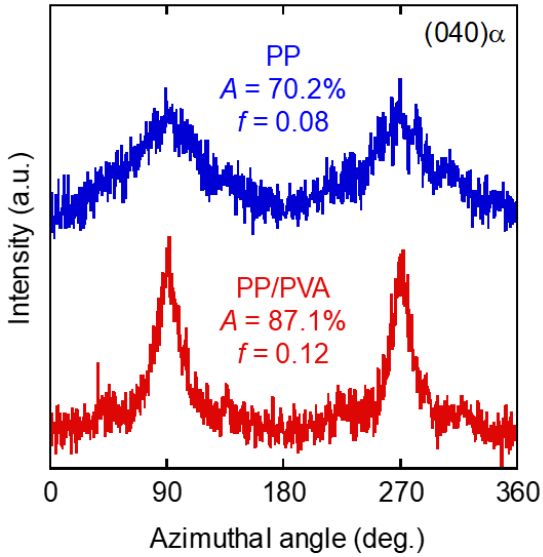

Fig. 16. Azimuthal distributions of the (040) α plane in 2D-WAXD images of the injection-molded specimens.

Molecular orientation was further assessed based on birefringence analyses using POM to evaluate the difference between the skin and core layers. Fig. 17 presents the POM images of a thin film acquired by slicing the sample parallel to the MD–ND plane. The distributions of the orientation function, F, are indicated in Fig. 18 as calculated from the birefringence via the equation:

$$F = \frac{\Delta n}{\Delta n_0}, \qquad (9)$$

where Δn is the birefringence and Δn_0 is the intrinsic birefringence, with a value of 0.040 [52]. Figs. 17 and 18 confirm that the PP/PVA exhibited significant orientation birefringence in the skin layer that was thicker than that of the PP (approximately 300 μm for the PP as opposed to 400 μm for the PP/PVA). This high level of molecular orientation correspond to the results obtained from the 2D-WAXD analysis.

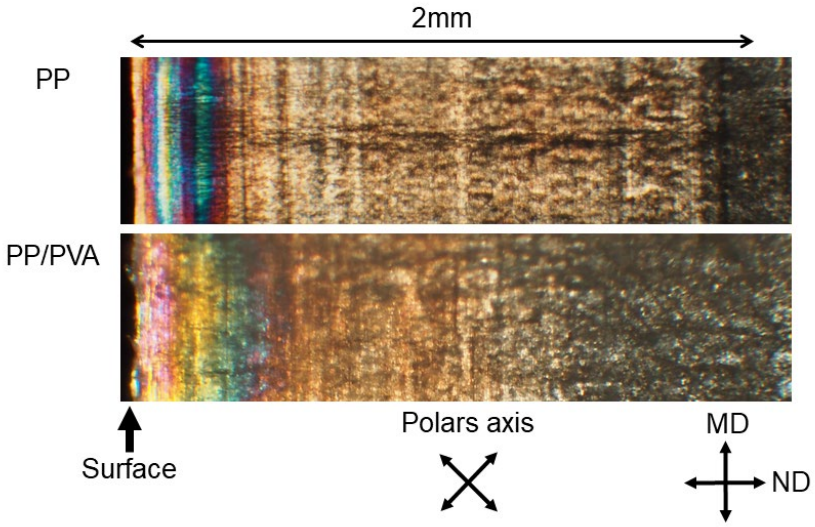

Fig. 17. POM images (crossed polars configuration) obtained from slices acquired parallel to the MD–ND plane of each injection-molded specimen.

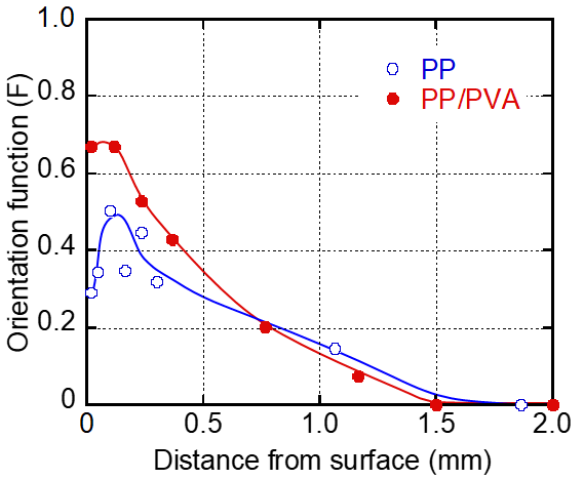

Fig. 18. Distributions of the orientation function, *F*, calculated from orientation birefringence data obtained from thin slices taken parallel to the MD–ND plane of each injection-molded specimen.

The crystallization behaviors of PP chains on the PVA fibers in the injection-molded specimens were observed using POM with a crossed polars configuration and inserting a full-wave plate at 130 °C to confirm the effect of the PVA fibers on the PP chain orientation. After holding the sample at 180 °C, for 10 min to melt the PP completely, the material was cooled to 130 °C. In these trials, the time to reach 130 °C was set to 0 s. The PVA fibers were found to have small optical retardation, suggesting that the PVA chains in these fibers were not highly orientated. The orientation direction of the PVA fibers is denoted by an arrow in Fig. 19. This directionality remained even in the molten PP, because additional pressure was not applied after melting the PP at 180 °C. Moreover, disturbance of the fiber orientation via Brownian motion is not expected because of the large fiber diameter (~5 μm). As shown in the figure, spherulites randomly appeared after 20 s in the pure PP, whereas PP chains crystallized parallel to the long axes of the PVA fibers in the PP/PVA. Furthermore, after crystallization was complete, a spherulite texture was observed in the pure PP. In contrast, highly oriented PP crystals with a homogeneous retardation were observed in the PP/PVA, such that the PP chains were oriented parallel to the long axis of the fibers. These results suggest that transcrystallization occurred at the fiber surfaces, as is often the case in fiber-reinforced plastics [53–57]. Furthermore, during the injection-molding, the geometry confinement effect (i.e., the orientation match between the PP chains and the PVA fibers) increased the number of nucleation sites available for the crystallization of the PP chains on the PVA fibers, since the actual surface area of the PVA fibers is enlarged. Because of the well-developed

transcrystalline structure, highly oriented PP chains were present in the injection-molded PP/PVA specimen.

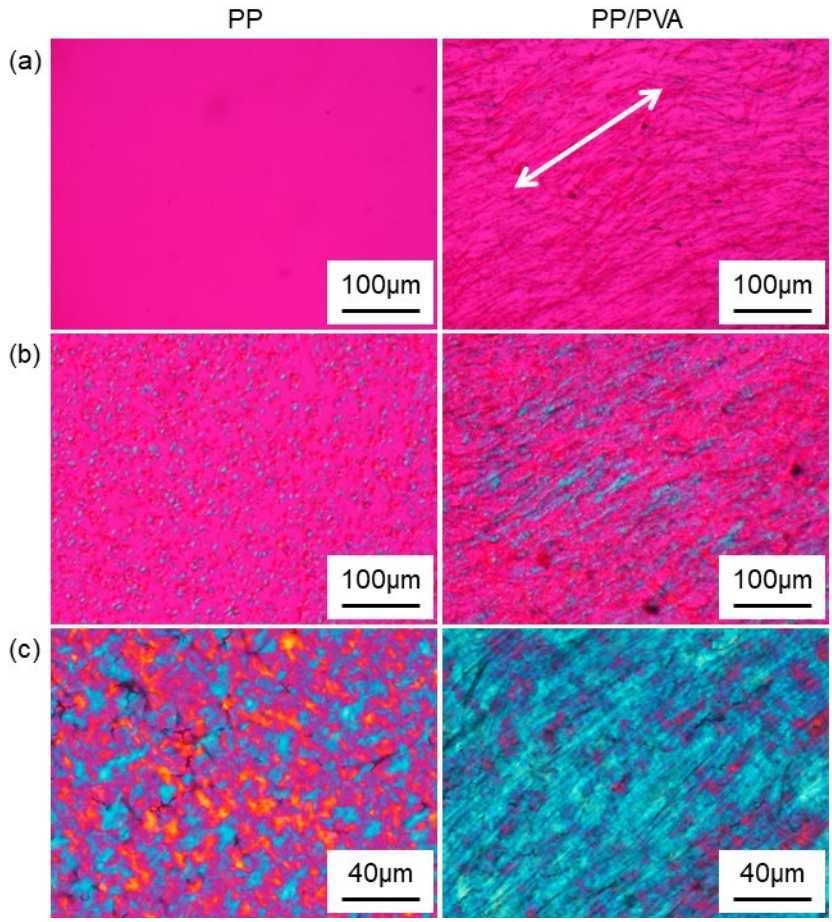

Fig. 19. POM images (crossed polars configuration and inserting a full-wave plate) of PP/PVA during isothermal crystallization at 130 ℃ after (a) 0 s and (b) 20 s, and (c) samples after crystallization was complete.

3.3 Mechanical and thermal properties of the injection-molded specimens

The high degree of chain orientation in the blended material evidently affected the mechanical properties of the product. Fig. 20 summarizes the temperature dependence of the dynamic tensile moduli, such as storage modulus, E', and loss modulus, E'', and the loss tangent, tan δ, at 10 Hz. The solution cast PVA film, which had no particular orientation, was also

assessed for comparison purposes. Owing to the increased molecular orientation of the PP chains and the high modulus of the PVA, the PP/PVA specimen had a higher E' than the pure PP specimen in the MD. The temperature for peak β-dispersion for the PP (approximately 10 °C) was not affected by the addition of PVA, which is expected because the two polymers are immiscible. The decrease in the maximum tan δ for the PP/PVA specimen is ascribed to the decrease in the PP fraction in this material and is in agreement with the initial DSC heating curves. Another peak of tan δ appeared at approximately 50 °C for both the PVA film and the PP/PVA specimen, presumably as a result of the glass-to-rubber transition of the PVA. Therefore, in the temperature range between the glass transition temperatures of the PP and PVA, the E' of the PP/PVA specimen was higher than that of the pure PP.

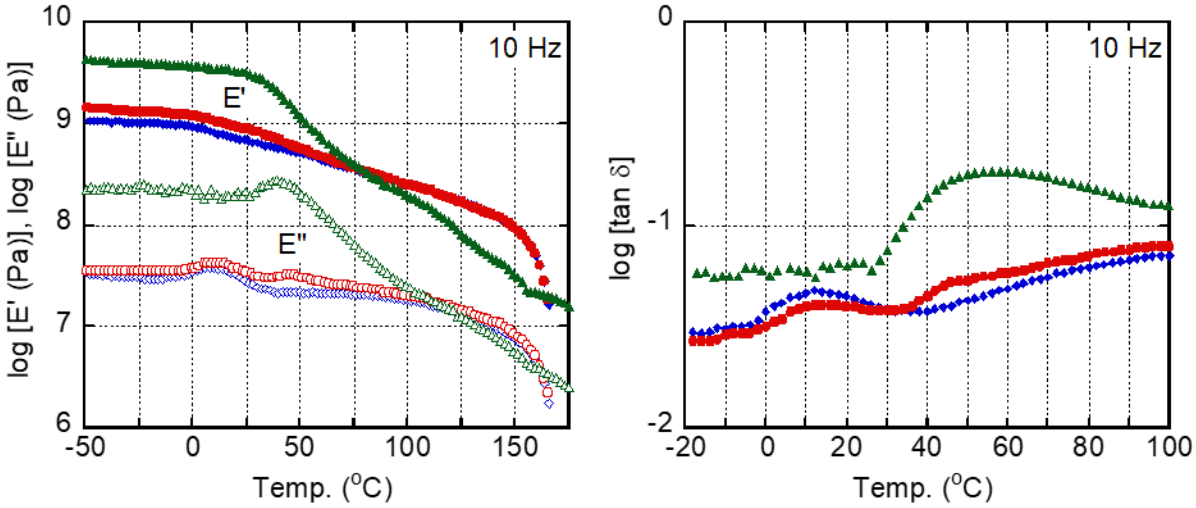

Fig. 20. The temperature dependence of the tensile storage modulus, E', tensile loss modulus, E'' (left), and loss tangent, tan δ (right), at 10 Hz for a PVA film (green triangles) and injection-molded specimens made of PP (blue diamonds) and PP/PVA (90/10) (red circles).

The stress–strain curves acquired at 23 °C are shown in Fig. 21. Both stress and strain are engineering values. In accordance with the dynamic mechanical properties of these same

materials, the tensile modulus of the PP/PVA (2.06 GPa) was significantly higher than that of the pure PP (1.50 GPa). Moreover, the yield stress of the PP/PVA (38.1 MPa) was higher than that of the PP (35.3 MPa), and the former also showed a lower yield strain. Thus, because of the high stress applied to the PP/PVA, this specimen had a low elongation at break. These properties are typical for rigid plastics and demonstrate that the addition of PVA fibers greatly enhanced the rigidity of the PP. The high modulus of the oriented PVA fibers and the molecular orientation of the PP chains are considered to be responsible for these results.

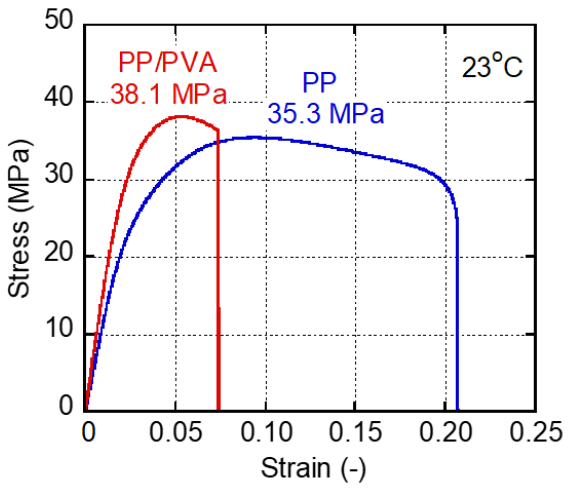

Fig. 21. Stress–strain curves obtained from tensile testing of injection-molded specimens.

The stress–strain curves obtained from three-point bending tests are presented in Fig. 22. As with the tensile tests, the flexural modulus and flexural strength were greatly enhanced by the addition of the PVA fibers. The results of the mechanical tests are summarized in Table 2.

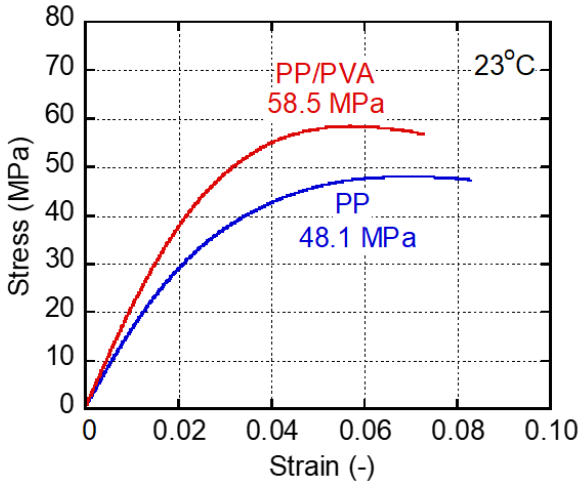

Fig. 22. Stress–strain curves obtained from bending tests of the injection-molded specimens.

Table 2. Mechanical properties of the injection-molded specimens.

	PP	PP/PVA (90/10)
Tensile modulus (GPa)	1.50 (0.01)	2.06 (0.01)
Tensile yield stress (MPa)	35.3 (0.17)	38.1 (0.14)
Flexural modulus (GPa)	1.64 (0.01)	2.14 (0.01)
Flexural strength (MPa)	48.1 (0.12)	58.5 (0.21)

(standard deviation)

The heat distortion temperature (HDT) values of the injection-molded specimens were evaluated under a pressure of 1.8 MPa and the HDT of the PP/PVA (61.5 °C) was found to be much higher than that of the PP (53.8 °C). This is attributed to the enhanced rigidity resulting from the high level of orientation in the former material.

In the present study, we prepared the composite with 10 % of PVA, which was the maximum amount of PVA due to the capability of the pump used to inject the PVA solution. In future, however, the samples with more PVA fibers can be prepared, which may further enhance the mechanical and thermal properties.

4. CONCLUSIONS

This study developed a novel technique for the production of polymer composites comprising PVA fibers in PP (a conventional hydrophobic plastic) using a twin-screw extruder. In this process, an aqueous solution of PVA was directly injected into molten PP from a liquid-injection nozzle and, after mixing, the water in the material was evaporated from a wide venting port. The PVA fibers were found to be homogeneously distributed in the PP without any agglomeration of PVA in the extrudates. Furthermore, no bubbles were detected, demonstrating that all the water had evaporated from the venting port. The resulting composite was injection-molded into dumbbell-shaped specimens that were used to evaluate the effects of adding PVA on the structure and properties of the composite. The PVA fibers, which acted as nucleating agents for the PP, were determined to be aligned parallel to the flow direction, such that the PP chains were highly oriented. These structural characteristics are responsible for the high modulus and high yield stress observed during tensile and bending deformations, as well as the elevated HDT of the product. The density of these PVA fibers is much lower than those of glass or carbon fibers, and so the technique described herein could potentially be used to produce new fiber-reinforced plastics with increased rigidity.

■ ACKNOWLEDGMENTS

A part of this work was supported by JSPS KAKENHI (grant number 18K19109). The authors would like to express their gratitude to the Nanotechnology Platform Program

(Molecule and Material Synthesis) of the Ministry of Education, Culture, Sports, Science, and Technology (MEXT) of Japan for technical support.

■ REFERENCES

[1] O. Demircan, T. Kosui, S. Ashibe, A. Nakai, Effect of surface treatment and twisting on tensile and bending properties of aramid unidirectional composites, Compos. Interfaces. 21 (2014) 287–299.

[2] Z. Shao, A. Nakai, S. Okubayashi, A simplified measurement of adhesion between p-aramid fiber and polypropylene, J. Text. Inst. 105 (2014) 129–135.

[3] H. Ozaki, M. Nakada, K. Uzawa, Y. Miyano, Effect of stamping condition on age deformation of textile carbon fiber reinforced polycarbonate laminates, J. Reinf. Plast. Compos. 34 (2015) 19–27.

[4] T. Matsuo, K. Kageyama, Compressive failure mechanism and strength of unidirectional thermoplastic composites based on modified kink band model, Compos. Part A. 93 (2017) 117–125.

[5] M. Nakada, Y. Miyano, Y. Morisawa, H. Nishida, Y. Hayashi, K. Uzawa, Prediction of statistical life time for unidirectional CFRTP under creep loading, J. Reinf. Plast. Compos. 38 (2019) 938–946.

[6] J. Koyanagi, N. Itano, M. Yamamoto, K. Mori, Y. Ishida, T. Bazhirov, Evaluation of the mechanical properties of carbon fiber/polymer resin interfaces by molecular simulation, Adv. Compos. Mater. 26 (2019) DOI:10.1080/09243046.2019.1630069.

[7] P. Pötschke, T.D. Fornes, D.R. Paul, Rheological behavior of multiwalled carbon nanotube/polycarbonate composites, Polymer. 43 (2002) 3247–3255.

[8] H. Yoon, K. Okamoto, M. Yamaguchi, Carbon nanotube imprinting on a polymer surface, Carbon. 47 (2009) 2840–2846.

[9] J.E.K. Schawe, P. Pötschke, I. Alig, Nucleation efficiency of fillers in polymer crystallization studied by fast scanning calorimetry: Carbon nanotubes in polypropylene, Polymer. 116 (2017) 160–172.

[10] R. Wiwattananukul, B. Fan, M. Yamaguchi, Improvement of rigidity for rubber-toughened polypropylene via localization of carbon nanotubes, Compos. Sci. Technol. 141 (2017) 106–112.

[11] I.A. Kinloch, J. Suhr, J. Lou, R.J. Young, P.M. Ajayan, Composites with carbon nanotubes and graphene: An outlook, Science. 362 (2018) 547–553.

[12] R. Nishikawa, M. Yamaguchi, Effect of carbon nanotube addition on structure and properties for extrudates of high-density polyethylene, J. Appl. Polym. Sci. 136 (2019) 48010/1–48010/8.

[13] K. Uetani, H. Yano, Zeta potential time dependence reveals the swelling dynamics of wood cellulose nanofibrils, Langmuir. 28 (2012) 818–827.

[14] V.K. Thakur, M.K. Thakur, Processing and characterization of natural cellulose fibers/thermoset polymer composites, Carbohydr. Polym. 109 (2014) 102–117.

[15] R. Ning, M. Takeuchi, C. Wu, T. Saito, A. Isogai, Preparation and characterization of zinc oxide/TEMPO-oxidized cellulose nanofibril composite films, Cellulose. 24 (2017) 4861–4870.

[16] M. Tenma, M. Yamaguchi, Structure and properties of injection-molded polypropylene with sorbitol-based clarifier, Polym. Eng. Sci. 47 (2007) 1441–1446.

[17] D. Liu, X. Li, H. Song, P. Wang, J. Chen, Q. Tian, L. Sun, L. Chen, B. Chen, J. Gong, G. Sun, Hierarchical structure of MWCNT reinforced semicrystalline HDPE composites: A contrast matching study by neutron and X-ray scattering, Eur. Polym. J. 99 (2018) 18–26.

[18] P. Phulkerd, T. Nakabayashi, S. Iwasaki, M. Yamaguchi, Enhancement of drawdown force in polypropylene containing nucleating agent, J. Appl. Polym. Sci. 136 (2019) 47295/1–47295/7.

[19] I. Sakurada, Polyvinyl Alcohol Fibers, Marcel Dekker, New York, 1985.

[20] B. Xu, H.A. Toutanji, J. Gilbert, Impact resistance of poly(vinyl alcohol) fiber reinforced high-performance organic aggregate cementitious material, Cem. Concr. Res. 40 (2010) 347–351.

[21] Y. Zhang, Z. Zhang, Z. Liu, Graphite coated PVA fibers as the reinforcement for cementitious composites, Mater. Res. Express. 5 (2018) 025206/1–025206/6.

[22] J. Wang, Q. Dai, R. Si, S. Guo, Investigation of properties and performances of Polyvinyl Alcohol (PVA) fiber-reinforced rubber concrete, Constr. Build. Mater. 193 (2018) 631–642.

[23] J. Jang, D.K. Lee, Oxygen barrier properties of biaxially oriented polypropylene/polyvinyl alcohol blend films, Polymer. 45 (2004) 1599–1607.

[24] N.T. Phong, M.H. Gabr, K. Okubo, B. Chuong, T. Fujii, Improvement in the mechanical performances of carbon fiber/epoxy composite with addition of nano-(Polyvinyl alcohol) fibers, Compos. Struct. 99 (2013) 380–387.

[25] X. Yan, A. Cayla, E. Devaux, F. Salaün, Microstructure evolution of immiscible PP-PVA blends tuned by polymer ratio and silica nanoparticles, Polymers. 10 (2018) 1031/1–1031/17.

[26] L. Sobczak, M. Jerabek, T. Lummerstorfer, D. Salaberger, K. Renner, A. Haider, Pseudo-ductile behavior of poly(vinyl alcohol) fiber-reinforced polypropylene, Polym. Compos. 40 (2019) 4067–4078.

[27] H.E.H. Meijer, J.M.H. Janssen, P.D. Anderson, Mixing of Immiscible Liquids, in: I. Manas-Zloczower (Ed.), Mixing and Compounding of Polymers, second ed., Hanser, Munich, 2009: pp. 41–182.

[28] M.-F. Boyaud, A. Aït-Kadi, M. Bousmina, A. Michel, P. Cassagnau, Organic short fibre/thermoplastic composites: morphology and thermorheological analysis, Polymer. 42 (2001) 6515–6526.

[29] P. Cassagnau, A. Michel, New morphologies in immiscible polymer blends generated by a dynamic quenching process, Polymer. 42 (2001) 3139–3152.

[30] T. Yokohara, S. Nobukawa, M. Yamaguchi, Rheological properties of polymer composites with flexible fine fibers, J. Rheol. 55 (2011) 1205–1218.

[31] J. Seemork, T. Sako, M.A. Bin Md Ali, M. Yamaguchi, Rheological response under nonisothermal stretching for immiscible blends of isotactic polypropylene and acrylate polymer, J. Rheol. 61 (2017) 1–11.

[32] S.M. Lahalih, S.A. Akashah, F.H. Al-Hajjar, Development of degradable slow release multinutritional agricultural mulch film, Ind. Eng. Chem. Res. 26 (1987) 2366–2372.

[33] W. Zhang, X. He, C. Li, X. Zhang, C. Lu, X. Zhang, Y. Deng, High performance poly(vinyl alcohol)/cellulose nanocrystals nanocomposites manufactured by injection molding, Cellulose. 21 (2014) 485–494.

[34] R. Nishikawa, H. Yoon, M. Yamaguchi, Rheological evaluation of carbon nanotube redistribution in polymer melt, Nihon Reoroji Gakkaishi. 47 (2019) 105–110.

[35] M.A. Bin Md Ali, K. Okamoto, M. Yamaguchi, T. Kasai, A. Koshirai, Rheological properties for polypropylene modified by polytetrafluoroethylene, J. Polym. Sci. Part B Polym. Phys. 47 (2009) 2008–2014.

[36] C.W. Macosko, Rheology: Principles, Measurements, and Applications, Wiley, New York, 1994.

[37] M. Avrami, Kinetics of phase change. I: General theory, J. Chem. Phys. 7 (1939) 1103–1112.

[38] K. Harnisch, H. Muschik, Determination of the Avrami exponent of partially crystallized polymers by DSC- (DTA-) analyses, Colloid Polym. Sci. 261 (1983) 908–913.

[39] M. Mucha, Z. Królikowski, Application of DSC to study crystallization kinetics of polypropylene containing fillers, J. Therm. Anal. Calorim. 74 (2003) 549–557.

[40] C.E. Fernández, M. Bermúdez, A. Alla, M. Mancera, M.G. García-Martín, E. Benito, I. Roffé, J.A. Galbis, S. Muñoz-Guerra, Crystallization behavior of poly(ε-caprolactone)/layered double hydroxide nanocomposites, J. Appl. Polym. Sci. 116 (2010) 2515–2525.

[41] H.S. Bu, S.Z.D. Cheng, B. Wunderlich, Addendum to the thermal properties of polypropylene, Makromol. Chemie, Rapid Commun. 9 (1988) 75–77.

[42] J. Varga, β-Modification of isotactic polypropylene: preparation, structure, processing, properties, and application, J. Macromol. Sci. Part B. 41 (2002) 1121–1171.

[43] H. Huo, S. Jiang, L. An, J. Feng, Influence of shear on crystallization behavior of the β Phase in isotactic polypropylene with β-nucleating agent, Macromolecules. 37 (2004) 2478–2483.

[44] M. Yamaguchi, T. Fukui, K. Okamoto, S. Sasaki, Y. Uchiyama, C. Ueoka, Anomalous molecular orientation of isotactic polypropylene sheet containing, Polymer. 50 (2009) 1497–1504.

[45] P. Phulkerd, S. Arayachukeat, T. Huang, T. Inoue, S. Nobukawa, M. Yamaguchi, Melting point elevation of isotactic polypropylene, J. Macromol. Sci. Part B. 53 (2014) 1222–1230.

[46] P.C. Roozemond, T.B. Van Erp, G.W.M. Peters, Flow-induced crystallization of isotactic polypropylene: Modeling formation of multiple crystal phases and morphologies, Polymer. 89 (2016) 69–80.

[47] A. Turner-Jones, J.M. Aizlewood, D.R. Beckett, Crystalline forms of isotactic polypropylene, Macromol. Chem. Phys. 75 (1964) 134–158.

[48] J. Seemork, M. Siriprumpoonthum, Y. Lee, S. Nobukawa, M. Yamaguchi, Effect of die geometry on drawdown force of polypropylene at capillary extrusion, Adv. Polym. Technol. 34 (2015) 21477/1–21477/7.

[49] Z.W. Wilchinsky, Measurement of orientation in polypropylene film, J. Appl. Phys. 31 (1960) 1969–1972.

[50] M. Tanaka, R.J. Young, Molecular orientation distributions in uniaxially oriented poly(L-lactic acid) films determined by polarized raman spectroscopy, Macromolecules. 39 (2006) 3312–3321.

[51] S.A. Arvidson, S.A. Khan, R.E. Gorga, Mesomorphic-α-monoclinic phase transition in isotactic polypropylene: A Study of processing effects on structure and mechanical properties, Macromolecules. 43 (2010) 2916–2924.

[52] R. Russo, V. Vittoria, Determination of intrinsic birefringence of smectic phase in isotactic polypropylene, J. Appl. Polym. Sci. 60 (1996) 955–961.

[53] T.E. Sukhanova, F. Lednický, J. Urban, Y.G. Baklagina, G.M. Mikhailov, V. V. Kudryavtsev, Morphology of melt crystallized polypropylene in the presence of polyimide fibres, J. Mater. Sci. 30 (1995) 2201–2214.

[54] G. Bogoeva-Gaceva, A. Janevski, E. Mader, Nucleation activity of glass fibers towards iPP evaluated by DSC and polarizing light microscopy, Polymer. 42 (2001) 4409–4416.

[55] H. Li, S. Jiang, J. Wang, D. Wang, S. Yan, Optical microscopic study on the morphologies of isotactic polypropylene induced by its homogeneity fibers, Macromolecules. 36 (2003) 2802–2807.

[56] H. Quan, Z.-M. Li, M.-B. Yang, R. Huang, On transcrystallinity in semi-crystalline polymer composites, Compos. Sci. Technol. 65 (2005) 999–1021.

[57] S. Zhang, W. Lin, L. Zhu, C.-P. Wong, D.G. Bucknall, γ-Form transcrystals of poly(propylene) induced by individual carbon nanotubes, Macromol. Chem. Phys. 211 (2010) 1348–1354.